IJC
International Journal of Cancer

Identification of diagnostic metabolic signatures in clear cell renal cell carcinoma using mass spectrometry imaging

Kanchustambham Vijayalakshmi[1], Vishnu Shankar[2], Ryan M. Bain[1], Rosalie Nolley[3], Geoffrey A. Sonn[3], Chia-Sui Kao[4], Hongjuan Zhao[3], Robert Tibshirani[2], Richard N. Zare[1] and James D. Brooks[3]

[1]Department of Chemistry, Stanford University, Stanford, California
[2]Department of Biomedical Data Science and Statistics, Stanford University, Stanford, California
[3]Department of Urology, Stanford University, Stanford, California
[4]Department of Pathology, Stanford University, Stanford, California

Clear cell renal cell carcinoma (ccRCC) is the most common and lethal subtype of kidney cancer. Intraoperative frozen section (IFS) analysis is used to confirm the diagnosis during partial nephrectomy. However, surgical margin evaluation using IFS analysis is time consuming and unreliable, leading to relatively low utilization. In our study, we demonstrated the use of desorption electrospray ionization mass spectrometry imaging (DESI-MSI) as a molecular diagnostic and prognostic tool for ccRCC. DESI-MSI was conducted on fresh-frozen 23 normal tumor paired nephrectomy specimens of ccRCC. An independent validation cohort of 17 normal tumor pairs was analyzed. DESI-MSI provides two-dimensional molecular images of tissues with mass spectra representing small metabolites, fatty acids and lipids. These tissues were subjected to histopathologic evaluation. A set of metabolites that distinguish ccRCC from normal kidney were identified by performing least absolute shrinkage and selection operator (Lasso) and log-ratio Lasso analysis. Lasso analysis with leave-one-patient-out cross-validation selected 57 peaks from over 27,000 metabolic features across 37,608 pixels obtained using DESI-MSI of ccRCC and normal tissues. Baseline Lasso of metabolites predicted the class of each tissue to be normal or cancerous tissue with an accuracy of 94 and 76%, respectively. Combining the baseline Lasso with the ratio of glucose to arachidonic acid could potentially reduce scan time and improve accuracy to identify normal (82%) and ccRCC (88%) tissue. DESI-MSI allows rapid detection of metabolites associated with normal and ccRCC with high accuracy. As this technology advances, it could be used for rapid intraoperative assessment of surgical margin status.

Introduction

The increased incidence of Stage 1 renal cell carcinoma brought about by cross-sectional imaging has resulted in increasing use of nephron-sparing approaches for management, including partial nephrectomy (PN) and ablation procedures.[1] In PN, the incidence of positive surgical margins (PSMs) in patients with small renal masses varies from 0.1 to 7% and for advanced RCC patients, from 18 to 32%.[2,3] Although the impact of PSM on long-term survival in RCC remains controversial,[4] large observational studies have shown that PSMs are significantly associated with higher rates of local recurrence and worse overall survival independent of other predictors.[5–7] Despite the importance of surgical margin assessment, only 69% of surgeons performing open and 58% performing laparoscopic PN report using intraoperative frozen sections (IFSs).[8] In ablative procedures, frozen sections of core biopsies are sometimes used intraoperatively to confirm diagnosis at the outset of the procedure.[9] Low utilization of IFS is caused by both the long processing time (often 30 min or more) and relatively low accuracy. In cases with true positive margins detected on final

K.V.L. and V.S. contributed equally to this work
Ryan M. Bain's current address is: Dow Chemical Co., Midland, MI 48674
Additional Supporting Information may be found in the online version of this article.
Key words: clear cell renal cell carcinoma, nephrectomy, surgical margins, histopathology, electrospray ionization, metabolome
Abbreviations: 2D: two-dimension; AUC: area under the curve; ccRCC: clear cell renal cell carcinoma; DESI-MSI: desorption electrospray ionization mass spectrometry imaging; FA: fatty acid; H&E: hematoxylin and eosin; HIF-2α: hypoxia-inducible factor 2α; IFS: intraoperative frozen section; Lasso: least absolute shrinkage and selection operator; LTQ: linear trap quadrupole; OCT: optimal temperature cutting; PE: glycerophosphoethanolamine; PG: glycerophosphoglycerol; PI: glycerophosphoinositol; PN: partial nephrectomy; PS: glycerophosphoserine; PSM: positive surgical margin; ROC: receiving operator characteristic; TCA: tricarboxylic acid; TIC: total ion current
DOI: 10.1002/ijc.32843
History: Received 23 Aug 2019; Accepted 9 Dec 2019; Online 21 Dec 2019
Correspondence to: James D. Brooks, E-mail: jbrooks1@stanford.edu; or Richard N. Zare, E-mail: zare@stanford.edu

What's new?

Intraoperative frozen section (IFS) analysis is used in clear cell renal cell carcinoma (ccRCC) to confirm diagnosis during partial nephrectomy. Surgical margin evaluation using IFS analysis is time-consuming and unreliable, however, leading to relatively low utilization. Here, the authors evaluated the feasibility of using desorption electrospray ionization mass spectrometry imaging (DESI-MSI) in assessing ccRCC in core tissues. Their combined predictive model consisting of differentially expressed metabolites and the ratio of glucose to arachidonic acid could discriminate cancer *vs.* normal tissue with an accuracy of 85%. DESI-MSI thus demonstrates promise as a method to improve detection of positive surgical margins intraoperatively.

pathology, frozen sections are positive in only 15–30% of cases.[10,11] The intention of this work is to provide a proof of concept that IFS analysis using desorption electrospray ionization mass spectrometry imaging (DESI-MSI) can increase substantially the usefulness of this approach.

DESI-MSI has emerged as a promising approach for spatial characterization of the metabolome that can detect the presence of cancer rapidly on frozen sections.[12,13] DESI-MS is easy to use, operates under ambient conditions and can provide high-resolution characterization of metabolites (currently ~200 μm) in scan times of 1 min. Statistical tools, such as least absolute shrinkage and selection operator (Lasso), have allowed identification of a parsimonious set of metabolites from the large pool of molecules identified by DESI-MS that can distinguish normal from malignant tissues.[14–16] Our group has tested DESI-MSI in several malignancies including stomach,[17] pancreatic,[18] skin,[19] and prostatic neoplasms[20] and have identified metabolomic signatures that identify cancer with high sensitivity and specificity. In pancreatic cancer, a direct comparison of DESI-MSI detection with frozen sections exhibited that cases that were positive by DESI-MSI but negative by histology showed higher rates of recurrence, suggesting that DESI-MSI might provide additional information on surgical margins.[18] Recently, hand-held mass spectrometry probes that can be used intraoperatively have been developed using DESI and desorption ionization and are being tested in several malignancies.[21,22]

Renal cell carcinoma is not only common but also potentially lends itself to detection by metabolomic approaches because many initiating mutations affect metabolism.[23] To evaluate the feasibility of using DESI-MSI in assessing clear cell renal cell carcinoma (ccRCC) in core tissues, we analyzed 40 normal tumor pairs of ccRCC. We built a predictive model using 23 paired samples and validated its performance on an independent test set of 17 pairs. We found that DESI-MSI was able to distinguish between ccRCC and normal tissue with an accuracy of 85%, demonstrating promise as a method to improve detection of PSMs intraoperatively.

Material (Patients) and Methods

Ex vivo specimens were harvested from both benign and cancerous areas in subjects undergoing nephrectomy for kidney cancer under an Institutional Review Board (IRB)-approved protocol that allowed association of clinical data with specimens (IRB-13828). The samples were exposed to room temperature prior to snap freezing in liquid nitrogen for 30 min. Biosamples were stored at −80°C in sealed freezer boxes until ready to use. Cases were selected based on cancer type (i.e., ccRCC) denoted in the surgical pathology report. Cancerous and normal tissues were harvested based on gross appearance. All samples selected for DESI-MSI underwent frozen sectioning to confirm histology (cancer *vs.* normal) and exclude necrotic tissues. The diameter size of the coring tool is 8 mm (Stainless steel, autoclavable), purchased from Alabama Research and Development (Munford, AL). We have used disposable coring tool from Sklar Surgical Instruments (West Chester, PA) of same diameter. DESI-MSI analysis was performed on a training set of 23 paired, fresh-frozen, normal and ccRCC core specimens with an equal representation of indolent and aggressive cancer. For a test set, we performed DESI-MSI on 17 independent cases (Supporting Information Table S1). A 5-μm frozen section of each frozen tissue core sample was stained with hematoxylin and eosin (H&E), and then a 10-μm section was obtained immediately adjacent to the H&E section using a Leica CM1950 cryostat (Leica Biosystems) for DESI-MSI analysis.

Patient-informed consent

We have been collecting kidney tissues under an IRB-approved protocol (IRB-13828) with patient-informed consent at our institution for 20 years.

DESI-MSI analysis

The primary workflow of DESI-MSI analysis of tissues is provided in the Supporting Information Scheme S1. DESI-MSI is an ambient ionization imaging technique (i.e., all the measurements were carried out at room temperature and atmospheric pressure). Prior to the data acquisition, tissues were stored at −80°C in a freezer and dried for 20 min using a vacuum desiccator. Optimal cutting temperature (OCT) polymeric compound was used for tissue embedding prior to the frozen sectioning on a microtome cryostat. OCT is readily ionized in the positive ion mode, and the mass spectrum consists of interference from polymeric peaks separated by 22 mass-to-charge (m/z) units (Supporting Information Fig. S1). However, OCT interference is absent in negative ion mode which consists mostly of deprotonated species and chloride adducts, unlike positive ion mode DESI-MSI with protonated, sodiated, and potassiated adducts.

Experimental details of tissue imaging by DESI-MSI have been described elsewhere.[24,25] Briefly, DESI-MSI was performed in the negative ion mode (−5 kV) from *m/z* 50–1,000, using linear trap quadrupole (LTQ)-Orbitrap XL mass spectrometer (Thermo Fisher Scientific, www.thermofisher.com) coupled to a home-built DESI source and a two-dimensional (2D) motorized stage. Both normal and ccRCC tissues were raster scanned under impinging charged droplets generated from the electrospray nebulization of a histologically compatible solvent system, 1:1 (vol/vol) dimethylformamide/acetonitrile (flow rate 1 μl/min). The electrospray nebulization was assisted by using sheath gas nitrogen (N_2, 170 psi) and a high electric field of −5 kV. The spatial resolution of DESI-MSI, defined by the spray spot size, is ∼200 μm (Supporting Information Fig. S2). DESI-MSI of all tissue samples were carried out under identical experimental conditions, such as spray tip-to-surface distance ∼2 mm, spray incident angle of 55° and spray-to-inlet distance ∼5 mm. The MSI data were acquired using XCalibur 2.2 software (Thermo Fisher Scientific). The tissue samples after DESI-MSI analysis were subjected to histopathologic evaluation using H&E staining (Supporting Information Fig. S4).

DESI-MSI was performed on tissue sections by placing the glass microscope slides onto a custom 2D precision moving stage. Images were collected in a series of rows by coordinating linear motion of the moving stage (134.22 μm sec^{-1}) with the MS duty cycle. The MS duty cycle was defined by the scan parameters: *m/z* 50–1,000, injection time of 500 msec with 1 microscan, scan time 1.49 sec and automatic gain control was disabled. A lateral spatial resolution (*x*) of 200 μm was defined, upon completion of a row the moving stage resets to the original *x* position while stepping 200 μm in *y*. This process was repeated in order to acquire data from the entire tissue surface. Given tissue surface area 4 mm by 4 mm = 16 mm^2, the acquisition time per pixel is about 1.49 s, acquisition time per row is 0.49 min (less than a minute for linear scan) and the total acquisition time per tissue is 9.8 min. However, it is important to note that we acquired whole slide scans in order to acquire a large data set for model building and testing. Once a model is optimized, we have shown we can acquire linear scan data that distinguish tissue types (normal and cancer) in less than 1 min.[20]

Tandem-MS and high mass resolution analyses were performed by using the LTQ-Orbitrap XL (Thermo Fisher Scientific). Tandem-MS spectra were analyzed (Supporting Information Figs. S7–S10), and molecular assignments were compared to databases such as LipidMaps (www.lipidmaps.org/), MassBank (www.massbank.jp) and Metlin (https://metlin.scripps.edu/). The detected species were mostly deprotonated small metabolites related to the tricarboxylic acid (TCA) cycle, and deprotonated lipids including free fatty acids (FAs), fatty acid dimers, phosphatidic acids, and glycerophospholipids (Supporting Information Table S2).[20] Supporting Information provides details of experimental conditions (Supporting Information Figs. S1–S4) and molecular analysis (Supporting Information Figs. S7–S10). The 2D chemical maps of molecular ions such as glucose, arachidonic acid and glycerophospholipids were plotted using Biomap (Supporting Information Fig. S3). Using MSiReader software (version v1.00), each tissue DESI-MS image was normalized by the total ion current (TIC) and the raw data from each pixel were extracted for statistical analysis.

Statistical analysis

We used the baseline Lasso,[26] log-ratio Lasso[16] and a combined ridge regression linear model to select statistically significant molecular ion peaks in MSI profiles, and built a classifier that estimates the probability of an individual pixel in each tissue DESI-MS image to be normal or cancerous (ccRCC).[14,16] Our training and validation set consisted of 23 and 17 pairs of tissue, respectively, where each pair is extracted from a single patient. Within the training set (23 benign and 23 cancer tissues), we applied the Lasso method (binary-logistic regression with L1 penalty) using glmnet package in the CRAN R language library.[15] We initially used an unbiased statistical approach to fit both Lasso models, where leave-one-patient-out cross-validation builds an initial pixel-based Lasso binary classifier. Lasso selects only a sparse subset of molecular features for classification.

To account for the random effects influencing MS data, intensity of each metabolite was normalized by the TIC for the corresponding pixel (Supporting information Fig. S11).[27,28] A nearest-neighbor clustering method was used to collect all pixel intensities corresponding to the nearest molecular ion peak for feature selection. Leave-one-patient-out cross-validation was employed to obtain the Lasso tuning parameter[26] and evaluate its predictive accuracy. Due to the known molecular diversity of ccRCC, the log-ratio Lasso[16] was also used to find a sparse subset of features, each representing the ratio of relative intensities of two metabolites (Supporting Information Tables S4–S5). Supporting Information Table S4 reports all the metabolites for which pairwise ratios were considered in selecting a log-ratio Lasso model. The log-ratio Lasso maintains the sparsity from Lasso and is unaffected by the multiplicative scaling of each observation in DESI-MSI. The Lasso and log-ratio Lasso models have complementary strengths, as discussed below in Lasso analysis. To harness the strengths of both models, we then fit a combined linear ridge regression model including the selected molecular features from both Lasso and log-ratio Lasso and compared the performances of all three models in discriminating the cancer *vs*. normal tissue on a separate test set. Similar to the baseline Lasso model, this model was built using the glmnet package in CRAN R language library. Supporting Information Tables S3, S5 and S6 report the model coefficients for the baseline Lasso, log-ratio Lasso and combined models, respectively.

Data availability

The data that support the findings of our study are available from the corresponding authors upon request.

Results

Molecular imaging and metabolite identification characteristics of ccRCC

We performed DESI-MSI of 40 paired normal and ccRCC tissues in the negative ionization mode from *m/z* 50–1,000. In the low mass range (*m/z* 50–200), we found significant differences in the distribution and abundance of small metabolites related to the TCA cycle, reflecting the known altered metabolism of ccRCC (Fig. 1). Compared to normal tissue, ccRCC displayed a higher abundance of lactate (*m/z* 89.0247), glucose (*m/z* 179.0557), glutamate (*m/z* 146.0457), *N*-acetyl glutamate (*m/z* 187.0415), 2-hydroxy butyrate (*m/z* 103.0401) and a lower abundance of creatinine (*m/z* 112.9856), fumarate (*m/z* 115.0764) and succinate (*m/z* 117.0193).

Differences in peak abundance were also apparent in the mass range *m/z* 200–1,000 (Fig. 2). Compared to the normal tissue, ccRCC tissue shows higher abundance of glycerophosphoglycerol (PG) 34:1 (18:1/16:0; *m/z* 747.5160), PG 36:3 (18:2/ 18:1; *m/z* 771.5160), glycerophosphoinositol (PI) 38:4 (18:0/20:4; *m/z* 885.5470), PI 36:2 (18:2/18:0; *m/z* 861.5473), PI 34:1 (16:1/18:0; *m/z* 835.5316) and glycerophosphoserine (PS) 36:1 (18:1/18:0; *m/z* 788.5424). ccRCC tissue shows lower abundance of aminophospholipids such as glycerophosphoethanolamine (PE) 36:4 (16:0/20:4; *m/z* 722.5119), PE 40:6 (20:4/20:2; *m/z* 790.5458), PE 40:4 (18:0/22:4; *m/z* 794.5034), and PS 38:4 (18:0/20:4; *m/z* 810.5387) and PS 34:1 (16:0/18:1).

Compared to normal tissue, ccRCC showed strong ion signals for FA dimers observed at *m/z* 537.4871 (oleic acid + palmitic acid) and at *m/z* 563.5026 (oleic acid + oleic acid),

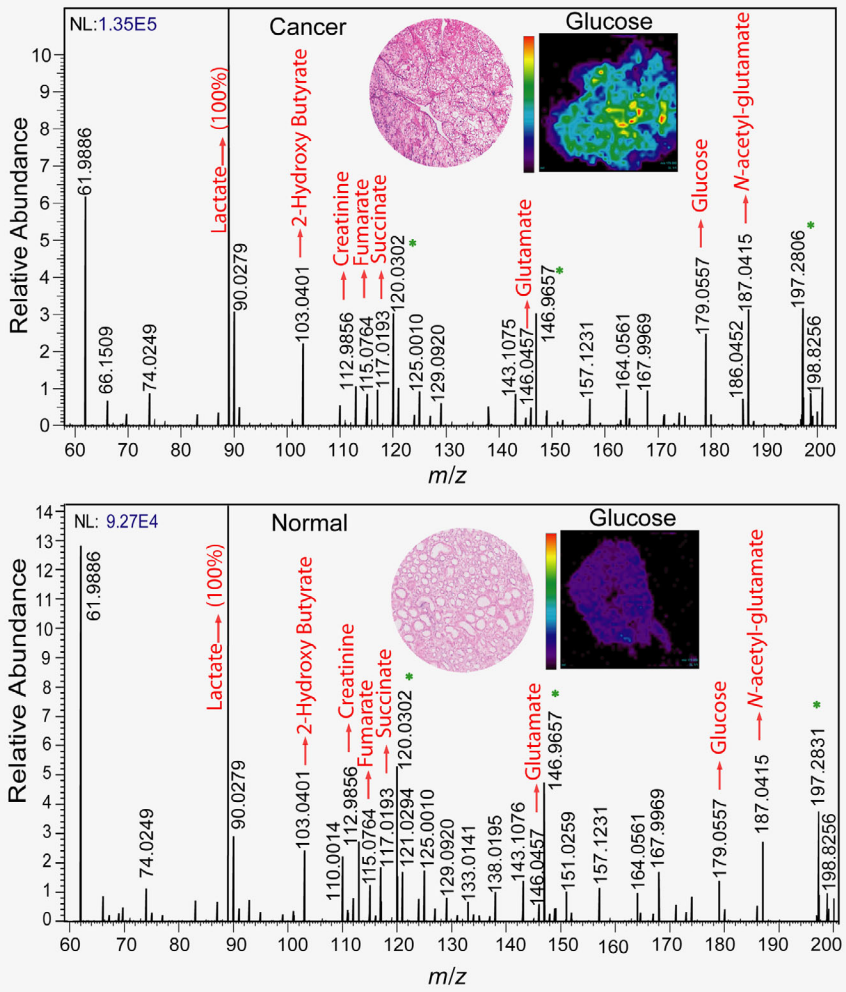

Figure 1. The comparison between MS profiles of normal *vs.* ccRCC tissue imaged at *m/z* 50–200. Inset shows the H&E images of ccRCC and normal tissue and the respective heat maps of the tissue plotted with respect to glucose. Peaks marked with an asterisk arise from background

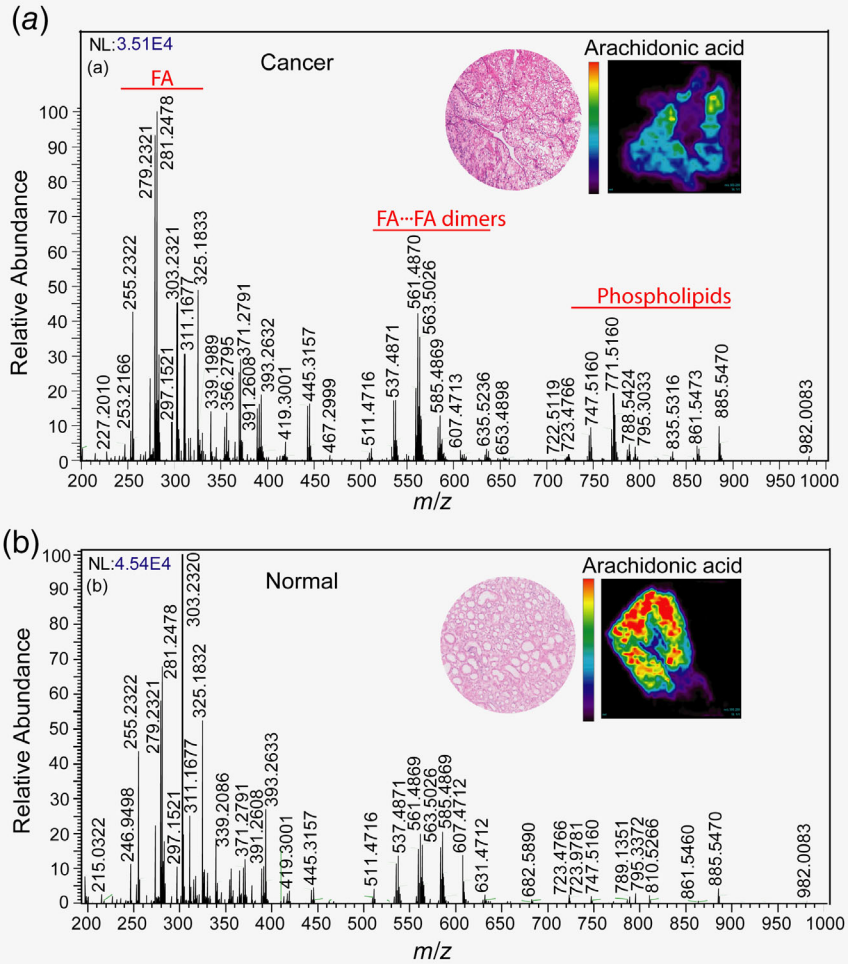

Figure 2. Comparison between MS profiles of normal *vs*. ccRCC tissue imaged at *m/z* 200–1,000. *Inset* shows the H&E images of ccRCC and normal tissue and the respective heatmaps of the tissue plotted with respect to arachidonic acid.

but not at *m/z* 585.4869 (oleic acid + arachidonic acid) and *m/z* 607.4013 (arachidonic acid + arachidonic acid). A higher abundance of fatty acids such as oleic acid FA (18:1; *m/z* 281.2478), linoleic acid FA (18:2; *m/z* 279.2321) and lower abundance of arachidonic acid FA (20:4; *m/z* 303.2320) was observed in ccRCC tissue. Other molecular ions that were distinctly different between normal and ccRCC tissues included palmitic acid (FA 16:0; *m/z* 255.2322), and unidentified metabolites *m/z* 311.1677, *m/z* 325.1833, *m/z* 339.1989, *m/z* 356.2795, *m/z* 371.2791, *m/z* 391.2608, *m/z* 393.2632, *m/z* 419.31001 and *m/z* 445.3157. The relative intensity distribution of each individual metabolite in ccRCC *vs.* normal tissue is shown in 2D chemical heat maps created using Biomap software (Supporting Information Fig. S2).

Lasso analysis

Three models were trained using the glmnet package in the CRAN R language library,[15] including the Lasso, log-ratio Lasso and a combined ridge regression model. The Lasso (binary logistic regression with L1 penalty) selects for a sparse set of 57 metabolites from 27,523 total detected molecular species across all 37,608 pixels in the training set. The average mass spectra are calculated for all pixels in training data (Supporting Information Fig. S5). It represents the change in the ccRCC tissue metabolism. Lasso coefficients were calculated for statistically significant features observed in the range *m/z* 50–1,000 (Supporting Information Fig. S6). The selected features from Lasso are noted in Supporting Information Table S3. The molecular ions with positive coefficients indicate a relatively higher amount of the respective metabolite in ccRCC compared to normal, and the molecular ions with negative coefficients are measured at lower amounts in ccRCC compared to normal tissue.

Previously, we have also found that a ratio of metabolites could be used to distinguish normal from malignant prostate tissues.[20] We therefore tested whether a ratio of metabolites could contribute to identification of ccRCC. To train the log-ratio Lasso model, it is computationally intractable to enumerate all possible ratios of relative intensities of molecular ions

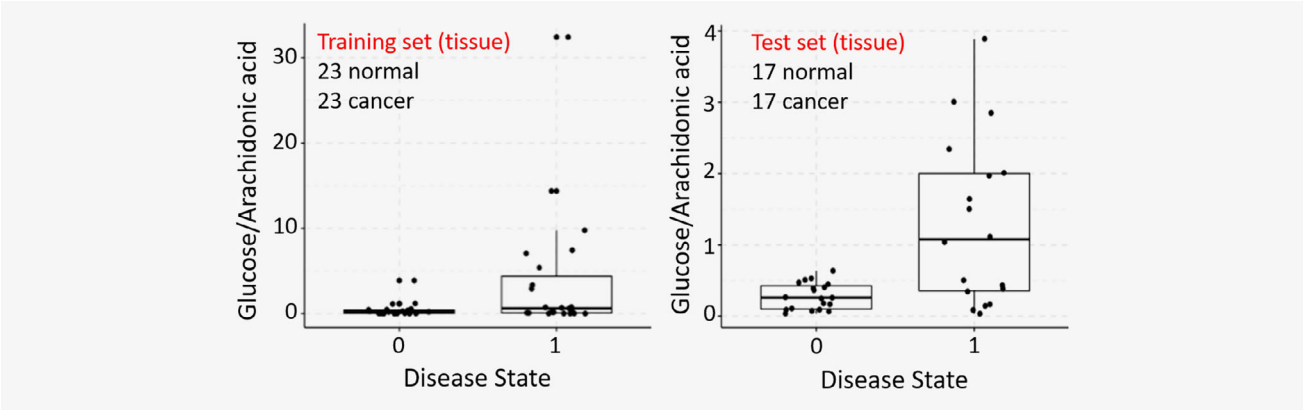

Figure 3. Comparison of relative intensity of ratio of glucose to arachidonic acid in normal tissue (0) and cancerous tissue (1). Each data point represents the average relative intensity of the ratio from all pixels in a tissue.

from 27,523 features (over 378 million ratios). We considered all pairwise ratios of 58 metabolites (total 1,653 features) that are known to be differentially expressed in cancer tissues from previous DESI-MSI studies (Supporting Information Table S4). Considering all pairwise ratios of 58 metabolites, the log-ratio Lasso model used leave-one-patient-out cross-validation to select one ratio (Supporting Information Tables S4 and S5). We found that the best ratio was glucose to arachidonic acid (Supporting Information Table S5). From the pixel-level to tissue-level classification, we employed a simple majority rule; if over 50% of pixels in a tissue were predicted to be cancerous, then the entire tissue was scored as cancerous.

From the cross-validation performance of both baseline Lasso and log-ratio Lasso on the training set, we found the accuracy to be 86.9 and 63.0%, respectively (Table 1). Lasso yielded a specificity (true negative rate) of 91.3% compared to the log-ratio model of 47.8%, while the sensitivity (true positive rate) of both models was comparable (82.6 and 78.3%).

Table 1. Leave-one-patient-out cross-validation performance of baseline Lasso, log-ratio Lasso on training sets and performance of all models on test set at tissue level

Set			**Predicted**		
Baseline Lasso			Normal	Cancer	% Agreement
Training (tissue)	Truth	Normal	21	2	91.3
		Cancer	4	19	82.6
Overall agreement 86.9%					
Log-ratio Lasso			Normal	Cancer	% agreement
Training (tissue)	Truth	Normal	11	12	47.8
		Cancer	5	18	78.3
Overall agreement 63.04%					
Baseline Lasso			Normal	Cancer	% agreement
Test (tissue)	Truth	Normal	16	1	94.1
		Cancer	4	13	76.5
Overall agreement 85.3%					
Log-ratio Lasso			Normal	Cancer	% agreement
Test (tissue)	Truth	Normal	9	8	52.9
		Cancer	1	16	94.1
Overall agreement 73.5%					
Combined model			Normal	Cancer	% agreement
Test (tissue)	Truth	Normal	14	3	82.4
		Cancer	2	15	88.2
Overall agreement 85.3%					

True negative rate (specificity) = (TN/[TN + FP]). True positive rate (sensitivity) = (TP/[TP + FN]).

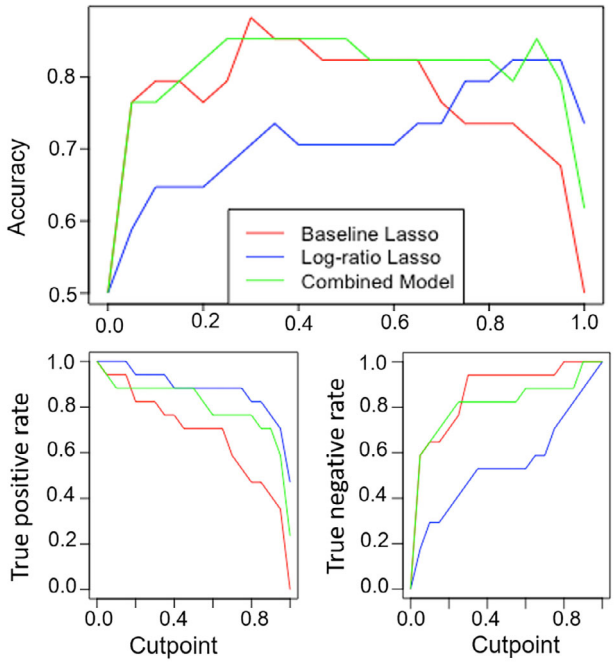

Figure 4. Sensitivity analysis to evaluate model accuracy, true positive, and true negative rates for various pixel to the tissue thresholds. This threshold (cut point) refers to the percentage of pixels required to be cancer positive for the overall tissue to be labeled as cancerous.

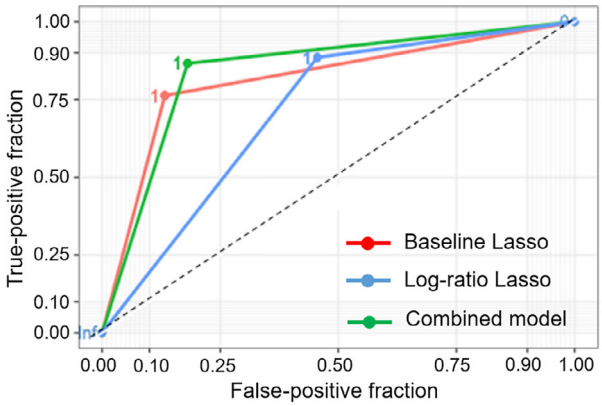

Model	Accuracy	Sensitivity	Specificity
Baseline Lasso	81.6 %	76.3%	86.7%
Log-ratio Lasso	70.9 %	88.5%	54.5%
Combined model	84.2 %	88.6%	81.9%

Figure 5. Comparison of three models using AUC and ROC curve at the pixel level. AUC metrics are 0.814, 0.714, and 0.842 for baseline, log-ratio, and combined models, respectively.

Although Lasso selected 57 peaks, spanning small metabolites, fatty acids, and lipids, it did not include either glucose or arachidonic acid. Therefore, it appeared that log-ratio Lasso model imparted unique information useful in distinguishing normal kidney tissue from ccRCC. The glucose/arachidonic acid ratio was a sensitive biomarker, where the ratio is elevated in cancer tissue (Fig. 3). However, the low log ratio observed in some cancers contributed to the low specificity shown in Table 1.

Finally, we observed that the Lasso and log-ratio Lasso had different strengths, with the former having higher specificity while the latter has higher sensitivity. Therefore, we included the selected features from both models (57 features from baseline Lasso and glucose/arachidonic acid ratio) in a ridge regression ("combined") model, which is optimized on the training set. This combined linear model was fit on all training set pixel data using ridge regression in the glmnet package.[15] We evaluated each model's performance at the pixel level on an independent test set of 17 pairs of tissues, using a majority rule from pixel to tissue-level classification. We also evaluated the sensitivity of all model performances to this pixel to tissue threshold, specifically what percent of pixels need to be cancerous for the overall tissue to be scored cancerous. Our sensitivity analysis (Fig. 4) finds that the combined model performance is most robust, because it maintains over 80% accuracy at the tissue level to changes in this threshold varying from 20 to 90%. This suggests our combined model may be clinically useful in predicting the tumor margins for tissues where the majority of pixels are cancer-free. With a 50% pixel to tissue threshold, we obtained an accuracy of 85.3, 73.5 and 85.3% at the tissue level for baseline Lasso, log-ratio model and the combined model, respectively (Table 1).

We further evaluated the performance of these models using the area under the curve (AUC) and receiving operator characteristic (ROC) curve (Fig. 5). The AUC metric for the baseline Lasso, log-ratio Lasso and combined models at the pixel level were 81.4, 71.4 and 84.2%, respectively. The AUC analysis demonstrated that the combined model had the best discriminative ability. The pixel-level performance of all three models was compared on the test set, where the combined model performs the best with 84.2% accuracy (compared to 81.6 and 70.9% accuracy of the baseline lasso and log-ratio models respectively). Our analysis shows that the combined approach harnessed both the sensitivity of the log-ratio Lasso and the specificity of the baseline Lasso to achieve classification accuracy and the highest AUC value.

Discussion

DESI-MSI is a label-free molecular imaging technique that probes the altered metabolism in cancer tissues. DESI-MSI has revolutionized the way by which metabolic profiling of tissues is performed *ex vivo* under ambient conditions and with minimal sample pretreatment. DESI-MS is currently being evaluated for near real-time identification of PSMs in glioblastoma,[29] and a hand-held mass spectrometry wand is being developed for intraoperative use.[21,22] We tested the

feasibility and accuracy of DESI-MS for distinguishing normal from malignant kidney tissues and found excellent performance characteristics, matching or exceeding those reported for frozen sections. Not only did we observe the expected differences in small metabolites related to the TCA cycle, we identified a number of lipid species that were altered in ccRCC. Our work provides a proof of concept for use of DESI-MSI to determine surgical margin status in ccRCC and reveals key metabolic differences between cancer and normal tissue consistent with the metabolic rewiring in ccRCC.

Achievement of negative surgical margins and preservation of renal function are key goals in PN. PSM rates are one of the key metrics used for evaluating quality in PN surgeries for RCC in both the United States and Europe.[30] Given that frozen sections are poorly sensitive, finding only 15–30% of PSMs disclosed on final pathology[10,11] and potentially increase ischemia time, many surgeons advocate against obtaining frozen sections.[4,10] However, performance of frozen sections is associated with lower rates of PSM on final pathology, and contemporary large studies have suggested that PSM influence cancer outcomes.[5–7] Furthermore, advances in surgical techniques have increased the number and complexity of cases amenable to PN.[31] The high accuracy of predicting cancer based on metabolites suggests that DESI-MS and mass spectrometry-based tools like a mass spectrometry pen that has been deployed intraoperatively in ovarian cancer with high accuracy for diagnosis.[32] DESI-MS can provide a rapid readout of diagnostic mass spectra that make it compatible with the goal of minimizing ischemia time and identifying PSM in the surgical bed. Such an enabling technology could facilitate safe expansion of indications for PN to more complex cases based on tumor size and location. Commercially available portable mass spectrometers with ion transfer tube coupled to the surgical pieces will enable incorporation of DESI-MSI in to the real-time analysis in the clinical setup.

The metabolites detected by DESI-MS coincide with known metabolic alterations in ccRCC that arise from alterations in hypoxia-sensing pathways induced by functional inactivation of the von Hippel–Lindau.[33,34] For example, we observed higher abundance of glucose and lactate, attributable to the upregulation of glucose transporter 1[35] and lactate dehydrogenase associated with a shift toward aerobic glycolysis.[36,37] Succinate and fumarate, members of the TCA cycle decrease with this metabolism shift, while glutamate increase, coinciding with induction of glutaminolysis.[34] Alterations in glutamine and more generally amino acid metabolism are indeed reflected by the statistical models, which select for *N*-acetyl aspartic acid, and *N*-acetyl glutamate peaks in the classification.

In addition, we find expected increases in fatty acids, fatty acid dimers and phospholipids and are able to identify quantitative increases in particular FAs and their dimers, such as palmitic acid (FA 16:0), linoleic acid (FA 18:2) and oleic acid (FA 18:1) and decreases in arachidonic acid (FA 20:4) and its dimers. Morphologically, ccRCC cells are lipid and glycogen laden,[38] likely reflecting the reprogramming of fatty acid and glucose metabolism known to occur in the development of ccRCC. Upregulation of fatty acid synthesis in ccRCC results in high concentrations of fatty acids, which can lead to the dimer formation in solvent droplets. DESI-MS of fatty acids profiles in the negative ion mode consists of abundant ions of deprotonated molecules, such as monomers $[M{-}H]^-$ and dimers $[2M{-}H]^-$. Dimers can be regarded as proton bound molecules $R\text{-}COO^- \cdots H^+ \cdots {}^-OOC\text{-}R$. The interaction can be due to electrostatic interactions (hydrogen bonds) between carboxylate anions and protons, or the hydrophobic interaction of fatty acids with longer aliphatic chains.[39]

Enzymes cyclooxygenase and lipoxygenase act on arachidonic acid to yield lipid mediators such as prostaglandins, thromboxane and leukotrienes. We observed 20-COOH–leukotriene B4 in ccRCC tissue (*m/z* 365.2454), a signal relay molecule in neutrophil chemotaxis to the inflammation sites (Supporting Information Fig. S8*h*).[40] In addition, other studies report that free polyunsaturated fatty acids such as FA (20:4) levels in ccRCC are strongly dependent on hypoxia-inducible factor 2α (HIF-2α) activity.[41] HIF-2α controls the fate of fatty acids either in phospholipid synthesis or in storage to form lipid droplets.[42] We observed elevated levels of PGs and PIs and suppressed aminophospholipids such as PSs and PEs. PEs are synthesized in mitochondria and are produced from the decarboxylation of PS synthesized in endoplasmic reticulum (ER).[43] The reduced levels of PS and PE can have profound effect on membrane trafficking of lipids and the asymmetric membrane structure, which in turn affect the programmed cell death apoptosis and phagocytosis.[44,45] Our DESI-MSI results suggest that ccRCC changes the lipidome, but still more needs to be learned about how different metabolic pathways are triggering tumorigenesis. In order to understand the roles of specific metabolites including specific fatty acids, and phospholipids, we and others are obtaining detailed information on the ccRCC metabolism.

Our study provides a proof of concept demonstrating the potential for using features of the metabolome for accurately distinguishing normal from malignant kidney ccRCC tissues. However, the performance characteristics could differ for other histologic subtypes of RCC including papillary, chromophobe and rare subtypes, as well as benign entities such as oncocytoma and angiomyolipoma.[46] Metabolic profiling and lipid profiling of RCC subtypes and ccRCC-derived metastases have a potential for the classification of subtypes and the identification of therapeutic targets.[47,48] We had a modest number of samples, although the large number of pixels per case provided sufficient power for robust model building. Additional work will also be necessary for optimization of the diagnostic calls for ccRCC to fit the clinical workflow. For example, as intraoperative mass spectrometry is incorporated into the workflow, it is likely that thresholds will need to be adjusted regarding the number of pixels used to make a call of malignancy as well as cutoffs for identifying cancer in our metabolite panel. Regardless, excellent

performance of our combined model on data show promise for considerable improvement in sensitivity for detecting cancer compared to present analysis of standard frozen sections. Finally, practical application of metabolic signatures will depend upon further development of technologies for portable and rapid mass spectrometry.

Conclusions

DESI-MSI is a promising technology for rapid analysis of tissue samples that can distinguish cancerous from normal kidney tissues. We have identified a wealth of new metabolites, including the lipidome, which can be used as diagnostic markers. This information can also be used to gain biological insights into ccRCC tumorigenesis. Our combined predictive model consisting of differentially expressed metabolites and the ratio of glucose to arachidonic acid can discriminate cancer *vs*. normal tissue with an accuracy of 85.3%. As rapid mass spectrometry methods become incorporated into the clinical workflow, our data strongly suggest that determination of surgical margins in many diseases, including RCC, will be a fruitful application with potential to improve clinical outcomes.

Acknowledgements

This work was funded by the National Institutes of Health, Grant CA229933.

Conflict of Interest

The authors declare no potential conflicts of interest.

References

1. Leppert JT, Mittakanti HR, Thomas IC, et al. Contemporary use of partial nephrectomy: are older patients with impaired kidney function being left behind? *Urology* 2017; 100:65–71.
2. Laganosky DD, Filson CP, Master VA. Surgical margins in nephron-sparing surgery for renal cell carcinoma. *Curr Urol Rep* 2017;18:8.
3. Orosco RK, Tapia VJ, Califano JA, et al. Positive surgical margins in the 10 Most common solid cancers. *Sci Rep* 2018;8:5686.
4. Dagenais J, Mouracade P, Maurice M, et al. Frozen sections for margins during partial nephrectomy do not influence recurrence rates. *J Endourol* 2018;32:759–64.
5. Shah PH, Moreira DM, Okhunov Z, et al. Positive surgical margins increase risk of recurrence after partial nephrectomy for high risk renal tumors. *J Urol* 2016;196:327–34.
6. Khalifeh A, Kaouk JH, Bhayani S, et al. Positive surgical margins in robot-assisted partial nephrectomy: a multi-institutional analysis of oncologic outcomes (leave no tumor behind). *J Urol* 2013; 190:1674–9.
7. Maurice MJ, Zhu H, Kim SP, et al. Reexamining the association between positive surgical margins and survival after partial nephrectomy in a large American cohort. *J Endourol* 2016;30:698–703.
8. Sidana A, Donovan JF, Gaitonde K. Surgeons' preferences and practice patterns regarding intraoperative frozen section during partial nephrectomy. *Urol Oncol* 2014;32:864–8.
9. Ramanathan R, Leveillee RJ. Ablative therapies for renal tumors. *Ther Adv Urol* 2010;2: 51–68.
10. Gordetsky J, Gorin MA, Canner J, et al. Frozen section during partial nephrectomy: does it predict positive margins? *BJU Int* 2015;116: 868–72.
11. Maruccia S, Seveso M, Casellato S, et al. The role for frozen section analysis during partial nephrectomy: outcomes after ten years of FU. *Eur Urol Suppl* 2017;16:e1369.
12. Ifa DR, Eberlin LS. Ambient ionization mass spectrometry for cancer diagnosis and surgical margin evaluation. *Clin Chem* 2016;62:111–23.
13. Chughtai K, Heeren RMA. Mass spectrometric imaging for biomedical tissue analysis. *Chem Rev* 2010;110:3237–77.
14. Tibshirani R. Regression shrinkage and selection via the Lasso. *J Roy Stat Soc Ser B* 1996;58: 267–88.
15. Friedman JH, Hastie T, Tibshirani R. Regularization paths for generalized linear models via coordinate descent. 2010;33:22.
16. Bates S, Tibshirani R. Log-ratio Lasso: scalable, sparse estimation for log-ratio models. *Biometrics* 2018;75:613–624.
17. Eberlin LS, Tibshirani RJ, Zhang J, et al. Molecular assessment of surgical-resection margins of gastric cancer by mass-spectrometric imaging. *Proc Nat Acad Sci* 2014;111:2436–41.
18. Eberlin LS, Margulis K, Planell-Mendez I, et al. Pancreatic cancer surgical resection margins: molecular assessment by mass spectrometry imaging. *PLoS Med* 2016;13:e1002108.
19. Margulis K, Chiou AS, Aasi SZ, et al. Distinguishing malignant from benign microscopic skin lesions using desorption electrospray ionization mass spectrometry imaging. *Proc Nat Acad Sci* 2018;115:6347–52.
20. Banerjee S, Zare RN, Tibshirani RJ, et al. Diagnosis of prostate cancer by desorption electrospray ionization mass spectrometric imaging of small metabolites and lipids. *Proc Nat Acad Sci* 2017;114:3334–9.
21. Zhang J, Rector J, Lin JQ, et al. Nondestructive tissue analysis for ex vivo and in vivo cancer diagnosis using a handheld mass spectrometry system. *Sci Trans Med* 2017;9:eaan3968.
22. Balog J, Sasi-Szabó L, Kinross J, et al. Intraoperative tissue identification using rapid evaporative ionization mass spectrometry. *Sci Trans Med* 2013;5:194ra93.
23. Linehan WM, Bratslavsky G, Pinto PA, et al. Molecular diagnosis and therapy of kidney cancer. *Ann Rev Med* 2010;61:329–43.
24. Eberlin LS, Ferreira CR, Dill AL, et al. Desorption electrospray ionization mass spectrometry for lipid characterization and biological tissue imaging. *Biochim Biophys Acta Mol Cell Biol Lipids* 2011;1811:946–60.
25. Eberlin LS. DESI-MS imaging of lipids and metabolites from biological samples. In: Raftery D, ed. *Mass Spectrometry in Metabolomics: Methods and Protocolsed*. New York, NY: Springer New York, 2014. 299–311.
26. Tibshirani R. Regression shrinkage and selection via the Lasso: a retrospective. *J Roy Stat Soc Ser B* 2011;73:273–82.
27. Deininger S-O, Cornett DS, Paape R, et al. Normalization in MALDI-TOF imaging datasets of proteins: practical considerations. *Anal Bioanal Chem* 2011;401:167–81.
28. Meuleman W, Engwegen JY, Gast M-CW, et al. Comparison of normalisation methods for surface-enhanced laser desorption and ionisation (SELDI) time-of-flight (TOF) mass spectrometry data. *BMC Bioinf* 2008;9:88.
29. Pirro V, Alfaro CM, Jarmusch AK, et al. Intraoperative assessment of tumor margins during glioma resection by desorption electrospray ionization-mass spectrometry. *Proc Nat Acad Sci* 2017;114:6700–5.
30. Campbell S, Uzzo RG, Allaf ME, et al. Renal mass and localized renal cancer: AUA guideline. *J Urol* 2017;198:520–9.
31. Marszalek M, Carini M, Chlosta P, et al. Positive surgical margins after nephron-sparing surgery. *Eur Urol* 2012;61:757–63.
32. Sans M, Zhang J, Lin JQ, et al. Performance of the MasSpec pen for rapid diagnosis of ovarian cancer. *Clin Chem* 2019;65:674–83.
33. Hakimi AA, Reznik E, Lee C-H, et al. An integrated metabolic atlas of clear cell renal cell carcinoma. *Cancer Cell* 2016;29:104–16.
34. Wettersten HI, Aboud OA, Lara PN Jr, et al. Metabolic reprogramming in clear cell renal cell carcinoma. *Nat Rev Nephrol* 2017;13:410–9.
35. Ambrosetti D, Dufies M, Dadone B, et al. The two glycolytic markers GLUT1 and MCT1 correlate with tumor grade and survival in clear-cell renal cell carcinoma. *PLoS One* 2018;13: e0193477.
36. Girgis H, Masui O, White NM, et al. Lactate dehydrogenase a is a potential prognostic marker in clear cell renal cell carcinoma. *Mol Cancer* 2014;13:101.
37. Courtney KD, Bezwada D, Mashimo T, et al. Isotope tracing of human clear cell renal cell carcinomas demonstrates suppressed glucose

oxidation *in vivo*. *Cell Metab* 2018;28:793–800.e2.
38. Gebhard RL, Clayman RV, Prigge WF, et al. Abnormal cholesterol metabolism in renal clear cell carcinoma. *J Lipid Res* 1987;28:1177–84.
39. Frański R, Gierczyk B, Schroeder G, et al. Do hydrophobic interactions exist in the gas phase? *Rapid Commun Mass Spect* 2008;22:1339–43.
40. Afonso PV, Janka-Junttila M, Lee YJ, et al. LTB4 is a signal-relay molecule during neutrophil chemotaxis. *Dev Cell* 2012;22:1079–91.
41. Zou Y, Palte MJ, Deik AA, et al. HIF-2α drives an intrinsic vulnerability to ferroptosis in clear cell renal cell carcinoma. *bioRxiv* 2018;388041.
42. Du W, Zhang L, Brett-Morris A, et al. HIF drives lipid deposition and cancer in ccRCC via repression of fatty acid metabolism. *Nat Commun* 2017;8:1769.
43. Tamura Y, Onguka O, Itoh K, et al. Phosphatidylethanolamine biosynthesis in mitochondria: phosphatidylserine (PS) trafficking is independent of a PS decarboxylase and intermembrane space proteins UPS1P and UPS2P. *J Biol Chem* 2012;287:43961–71.
44. Emoto K, Toyama-Sorimachi N, Karasuyama H, et al. Exposure of Phosphatidylethanolamine on the surface of apoptotic cells. *Exp Cell Res* 1997;232:430–4.
45. Saito K, Arai E, Maekawa K, et al. Lipidomic signatures and associated transcriptomic profiles of clear cell renal cell carcinoma. *Sci Rep* 2016;6:28932.
46. Dill AL, Eberlin LS, Zheng C, et al. Multivariate statistical differentiation of renal cell carcinomas based on lipidomic analysis by ambient ionization imaging mass spectrometry. *Anal Bioanal Chem* 2010;398:2969–78.
47. Leuthold P, Schaeffeler E, Winter S, et al. Comprehensive Metabolomic and Lipidomic profiling of human kidney tissue: a platform comparison. *J Prot Res* 2017;16:933–44.
48. Schaeffeler E, Büttner F, Reustle A, et al. Metabolic and Lipidomic reprogramming in renal cell carcinoma subtypes reflects regions of tumor origin. *Eur Urol Focus* 2019;5:608–18.